Fatigue microcrack detection with digital image correlation

Jérémie Rupil, Stéphane Roux, François Hild, Ludovic Vincent

Fatigue microcrack detection with digital image correlation

J. Rupil,[a,b] S. Roux,[a] F. Hild,[a] and L. Vincent[b]

[a]LMT Cachan, ENS Cachan/CNRS/UPMC/PRES UniverSud Paris,
61 avenue du Président Wilson, F-94235 Cachan cedex, France.

[b]CEA Saclay, DEN-DANS/DMN/SRMA/LC2M,
F-91191 Gif sur Yvette cedex, France.

August 18, 2011

Abstract

A digital image correlation method is proposed to detect and quantify automatically microcracks on the surface of a specimen during a fatigue test. The proposed procedure allows for a fast scanning of the entire surface with all possible (pixel-wise) locations of microcrack centers and the detection of cracks having a sub-pixel opening. An experimental test case is presented as an illustration of the method and a comparison with a replica technique is performed.

Keywords: Crack initiation; Digital image correlation; Mechanical fatigue; Microcrack detection.

1 Introduction

Many industrial structures are subjected to fatigue loadings. If the material has no initial bulk or surface defects, a cyclic loading level greater than the fatigue limit initiates microcracks [1]. The major part of damage growth consists of random multi-initiations of short cracks on the surface called herein microcracks, prior to the final growth of a main macrocrack. This random multiple initiation phenomenon is now well described in the literature [2, 3, 4]. However, at initiation, microcracks are short and have a small opening, so that their detection and quantification over a large area remain an experimental challenge. This difficulty leads to statistical analyses of fatigue tests based on failure (or at best large scale crack) statistics. Such approaches are time consuming and fragile as only the final (or late) results are accessible while initiations, competition, selection and growth of microcracks have to be inferred. Any progress in the early detection of microcracks gives access to a very rich information opening the way to a statistical analysis based on a single specimen, and to the validation of a crack growth scenario. To make the experimental challenge more concrete, in the present study based on a 304L stainless steel, the ultimate goal would be to detect microcracks whose extension is of a few grain sizes, say about 150 μm (a smaller size would be pointless), with an opening as small as 600 nm.

In this paper a dedicated digital image correlation technique is developed to address this challenge. This technique allows for the detection of very short cracks initiated during a fatigue test while only resorting to standard optical pictures captured *in situ* with a classical Digital Single Lens Reflex

(DSLR) camera during a fatigue test.

To monitor microcracking, the currently used procedures are often long to set up. As an example the replication technique with a polymer film, which provides a good resolution for crack detection and quantification [5], is a work intensive protocol. It consists in:

- placing the swollen polymer film on the sample surface;
- drying of the film, and extraction;
- plating of the replica with a conductive (metal) coating;
- observing the replica with a scanning electron microscope (or an optical microscope);
- identifying microcracks on images and performing geometrical measurements based on image analysis techniques.

Consequently, at least several hours are needed for a full analysis, and in the chain of elementary steps, different sources of error or uncertainty accumulate.

Alternative techniques exist based on an optical device (classical microscope [6], long distance microscope [7, 8, 9], DSLR camera with a high magnification lens [10], directly in front of the specimen. These experimental approaches proved to be efficient but detection and quantification are to be performed "manually." Moreover, most of the time the observed area is quite small (in order to have a good spatial resolution) although the use of the latest digital camera allows for the observation of larger areas (*i.e.,* several square millimeters).

In the present work, a Digital Image Correlation (DIC) method is proposed combining large areas of observation with a good spatial resolution and fast computation for crack detection and quantification. In the literature, DIC has already been used to detect and study cracks [11, 7, 12, 13, 14]. In most cases however, one (or a few) extended cracks are studied, with various opening levels. In the present case, the displacement field is analyzed in the presence of many microcracks. Along cracks, displacement discontinuities are expected. This signature is used for crack location and quantification. Hence, from the registration of two images (one being of the undamaged surface while the other one presents initiation of one or several microcracks) the method allows for the extraction, at low computational price, of several quantities such as the number of microcracks, their position and size. These data are estimated from each picture taken during the fatigue test. Finally, this technique leads to the description of fatigue damage evolution.

The paper is divided into five parts. In the first one, Section 2, the experimental procedure that leads to the capture of the raw pictures is described. The theoretical aspect of the method of crack detection is presented in Section 3 for a very general framework of sensitivity analysis, and its practical implementation for micro-crack detection in Section 4. The results are discussed and compared to more classical replication technique analyses and global correlation studies in Section 5. Finally, Section 6 recalls the main results.

2 Experimental procedure

2.1 Experimental setup

The global geometry of the specimen (Figure 1) is similar to classical fatigue samples. To monitor the damage steps with DIC, a gauge surface is obtained by machining a planar zone. This type of notched geometry has already been used successfully [8, 9] for observations of multiple crack initiations. The geometry was slightly modified to obtain a larger surface of observation. The shallow notch creates a local stress heterogeneity on the surface in order to localize initiation. The notched area is mechanically polished. A final electropolishing is performed resulting in a good quality of the surface finish suitable for optical observations. Figure 2(a) shows a microscopic observation carried out after surface polishing. DIC is performed from direct images of the polished surface without any further preparation or marking. It allows for a very early detection of microcracks. However, DIC is based on the assumption that the texture is simply advected by the local displacement without any further alteration (gray level or contrast modification). In the experimental study reported herein, this is not the case because of surface roughening due to the progressive formation of Persistent Slip Band (PSB) [15, 16, 17]. This induces a slight degradation of brightness conservation with fatigue cycles. The use of a more classical texture composed of droplets of black paint sprayed over a white background would prevent any detection of a crack before it breaks through the paint.

The present fatigue tests have been performed on an AISI 304L stainless steel. It is a polycrystalline austenitic steel (Figure 2(a)) containing residual

ferrite (approximatively 4 wt%) in the form of elongated grains. The average grain diameter is equal to 40 μm. Specimens are cycled by sine-wave loading (5-Hz frequency) in a servohydraulic testing machine. Stress amplitude $\Delta\sigma_{xx}/2$ is controlled for all the tested samples. Periodically, at maximum load, a picture is captured with a DSLR camera (CANON EOS 5D) and a macro lens (CANON MPE65) with a magnification of $\times 5$. The camera is triggered by the software used to control the testing machine. The data are gray level raw images with a resolution of approximately 3 Mpixels for a notch surface of 3×5 mm^2. The final pixel size on the raw pictures is 3.2 μm. The raw pictures (Figure 2(b)) could be directly used for crack detection but this requires that the crack opening reaches about a pixel size at least. Therefore, the detection of microcracks with a good spatial resolution is possible with the use of a DIC technique that enables for subpixel resolutions [18, 19]. Moreover, the use of DIC gives access to the quantification, in terms of size and opening, of the microcrack. The DIC technique presented here is then far more powerful than simply an imaging method on the raw pictures.

3 Full field crack detection technique

Even though all the images are captured at maximum load, the displacement maps show a gradient related to the cyclic softening of the material. Such a behavior is classically encountered with this kind of material (304L) and for the studied domain of fatigue lifetime (*i.e.,* more than 10,000 cycles). The cyclic behavior is composed of three phases, namely, primary hardening,

cyclic softening and finally secondary hardening [20, 21]. Since the behavior is never stabilized, two types of treatment need to be performed. The first one consists in the computation of a long wavelength displacement gradient through the whole image. The second for microcrack quantification is based on the detection of stress relaxation zones surrounding the microcracks inducing a displacement gradient at the local scale. The presented method is adapted to detect one single microcrack, and multiple parallel and independent microcracks.

3.1 Global DIC

A global DIC analysis allows to measure the displacement field, $\boldsymbol{U}$, through its decomposition over the basis $\boldsymbol{\Phi}_n$

$$\boldsymbol{U}(\boldsymbol{x}) = \sum_n a_n^0 \boldsymbol{\Phi}_n(\boldsymbol{x}) \tag{1}$$

where a_n^0 are the sought components, and $\boldsymbol{x}$ designates a current point of 2D spatial coordinates, namely, $\boldsymbol{x} = (x, y)$ in the Region of Interest (ROI).

Let $f(\boldsymbol{x})$ represent the *reference image* as the value of the gray level at each (discrete) point (pixel) of the image. The *deformed image* $g(\boldsymbol{x})$ is assumed to show the same texture as $f(\boldsymbol{x})$ translated by the local displacement field. Therefore, it is assumed that

$$f(\boldsymbol{x}) = g(\boldsymbol{x} + \boldsymbol{U}(\boldsymbol{x})) \tag{2}$$

with $\boldsymbol{U}(\boldsymbol{x})$ being the displacement field. This equation corresponds to the gray level conservation during the motion.

The deformed image $g(\boldsymbol{x})$ can be corrected by any trial displacement field $\boldsymbol{V}(\boldsymbol{x})$, defining the *corrected deformed image* $\hat{h}(\boldsymbol{x}) \equiv g(\boldsymbol{x} + \boldsymbol{V}(\boldsymbol{x}))$, so that f and $\hat{h}$ would coincide at convergence $\boldsymbol{V} = \boldsymbol{U}$. The DIC algorithm thus consists in an iterative scheme leading to an estimate $\boldsymbol{V}$ of $\boldsymbol{U}$, such that f and $\hat{h}$ match at best. This best match is to be understood in the least squares sense, so that the *global* residual

$$R_0^2 = \int_{\text{ROI}} [\hat{h}(\boldsymbol{x}) - f(\boldsymbol{x})]^2 \, \mathrm{d}\boldsymbol{x} \tag{3}$$

is minimized with respect to the degrees of freedom a_n^0.

The image correction step being non-linear, an iterative procedure is designed where the displacement field $\boldsymbol{V}^{(p)}$ at step p is progressively adjusted until convergence. The initial value of $h^{(0)}$ is equal to g itself (*i.e.,* no initial value is assumed for $\boldsymbol{V}$ in the present case). The corrected deformed image at step p is denoted by $\hat{h}^{(p)}(\boldsymbol{x})$. Using a first order Taylor expansion for $\hat{h}^{(p-1)}(\boldsymbol{x})$, and denoting by $\boldsymbol{\gamma}$ the image gradient, $\boldsymbol{\gamma} \equiv \nabla f$, the estimate $\hat{h}^{(p)}$ reads

$$\hat{h}^{(p)}(\boldsymbol{x}) \approx \hat{h}^{(p-1)}(\boldsymbol{x}) + \boldsymbol{\delta V}^{(p)}(\boldsymbol{x}) \cdot \boldsymbol{\gamma}(\boldsymbol{x}) \tag{4}$$

where the displacement field $\boldsymbol{\delta V}^{(p)}$ is the correction to apply to the current estimate $\boldsymbol{V}^{(p-1)}$. Since $\boldsymbol{V}^{(p-1)}$ and $\boldsymbol{\delta V}^{(p)}$ are decomposed over the basis $\boldsymbol{\Phi}_n$, the residual minimization leads to a linear system [22]

$$\mathbf{M} \cdot \boldsymbol{\delta a}^{(p)} = \boldsymbol{b}^{(p)} \tag{5}$$

with

$$M_{ij} = \int [\boldsymbol{\Phi}_i(\boldsymbol{x}) \cdot \boldsymbol{\gamma}(\boldsymbol{x})][\boldsymbol{\Phi}_j(\boldsymbol{x}) \cdot \boldsymbol{\gamma}(\boldsymbol{x})] \, \mathrm{d}\boldsymbol{x} \tag{6}$$

and

$$b_i^{(p)} = \int [\boldsymbol{\Phi}_i(\boldsymbol{x}) \cdot \boldsymbol{\gamma}(\boldsymbol{x})][f(\boldsymbol{x}) - \hat{h}^{(p-1)}(\boldsymbol{x})] \, \mathrm{d}\boldsymbol{x} \tag{7}$$

Vector $\boldsymbol{\delta a}^{(p)}$ represents the correction to the current estimate components $\boldsymbol{a}^{(p-1)}$ of the displacement $\boldsymbol{U}$ so that

$$\boldsymbol{a}^{(p+1)} = \boldsymbol{a}^{(p)} + \boldsymbol{\delta a}^{(p)} \tag{8}$$

With this new determination of the displacement field, an updated (*i.e.,* corrected) deformed image can be computed. This describes one iteration loop of the algorithm. Convergence is reached when the correlation residual R_0 no longer decreases.

3.2 Strategy

The strategy followed herein is first to analyze the long wavelength displacement field using a global DIC method [23, 24, 25, 22]. For this purpose a displacement basis consisting of rigid body motions and uniform strains is chosen, and the sought displacement field is decomposed over this basis. The key point is that it is made of a few functions $n = 1, ..., N$ of the order of 10 at most, so that the determination of the displacement field shows a very low uncertainty and error provided the kinematics is relevant. However, because of the regularity of the chosen fields, microcracks will not be revealed. They are expected to induce only local perturbations of the displacement field in their vicinity.

The second step of the procedure is a *sensitivity analysis*, namely, one additional degree of freedom (typically, that associated with the presence of a microcrack) is proposed, and its influence is evaluated. In terms of principle,

it is close to procedures based upon topological derivatives [26]. As compared to a global DIC computation this is a very modest problem with a *single* degree of freedom. Moreover, a unique iteration is performed so that this computation is extremely fast. However, a very large number of those degrees of freedom will be considered. As the location and size of the microcrack are unknown, it is proposed to scan all possible locations (at any pixel) of the proposed microcrack center, and all lengths. This is the reason why the resolution of the problem is not to be done accurately (including non-linear corrections), but rather it consists in probing the initial (single iteration) gain for a candidate field. Note that the first step is the direct application of a global DIC procedure, but the second step is an original algorithm that has never been proposed and hence the following sections provide details on this sensitivity analysis. First, the most general sensitivity analysis is presented. Then a simplification is proposed for local test functions. A fast scanning procedure is finally described for probing all positions of the test function.

3.3 Details of the sensitivity analysis

The sensitivity analysis consists in enriching a kinematic basis $\boldsymbol{\Phi}_n(\boldsymbol{x})$, $1 \leq n \leq N$, with the additional test function $\boldsymbol{\Phi}_{N+1}(\boldsymbol{x}) = \boldsymbol{\Psi}(\boldsymbol{x})$. Moreover, it is assumed that the deformed image g as been corrected to $\hat{h}$ by the displacement field as obtained from the initial N degrees of freedom.

Following the above global DIC procedure, the minimization of the en-

riched system consists in solving

$$\left[\begin{array}{cc} \mathbf{M} & \boldsymbol{N} \\ \boldsymbol{N}^t & P \end{array}\right] \left\{\begin{array}{c} \boldsymbol{a} \\ \chi \end{array}\right\} = \left\{\begin{array}{c} \mathbf{0} \\ c \end{array}\right\} \tag{9}$$

where

$$\begin{aligned} N_i &= \int [\boldsymbol{\Phi}_i(\boldsymbol{x}) \cdot \boldsymbol{\gamma}(\boldsymbol{x})][\boldsymbol{\Psi}(\boldsymbol{x}) \cdot \boldsymbol{\gamma}(\boldsymbol{x})] \, \mathrm{d}\boldsymbol{x} \\ P &= \int [\boldsymbol{\Psi}(\boldsymbol{x}) \cdot \boldsymbol{\gamma}(\boldsymbol{x})]^2 \, \mathrm{d}\boldsymbol{x} \\ c &= \int [\boldsymbol{\Psi}(\boldsymbol{x}) \cdot \boldsymbol{\gamma}(\boldsymbol{x})][f(\boldsymbol{x}) - \hat{h}(\boldsymbol{x})] \, \mathrm{d}\boldsymbol{x} \end{aligned} \tag{10}$$

Note that the first components of the second member are vanishing since the deformed image is assumed to be corrected by the first N degrees of freedom, so that if χ is forced to zero then $\boldsymbol{a} = \mathbf{0}$. It is straightforward to solve the linear system

$$\begin{aligned} \boldsymbol{a} &= -\frac{c\mathbf{M}^{-1}\boldsymbol{N}}{P - \boldsymbol{N}^t\mathbf{M}^{-1}\boldsymbol{N}} \\ \chi &= \frac{c}{P - \boldsymbol{N}^t\mathbf{M}^{-1}\boldsymbol{N}} \end{aligned} \tag{11}$$

The minimized residual (approximated through the usual linearity assumption [25, 22]) reads

$$R^2 = \frac{c^2}{2[P - \boldsymbol{N}^t\mathbf{M}^{-1}\boldsymbol{N}]} \tag{12}$$

Hence the quality gain is

$$G = R^2 = \frac{c\chi}{2} \tag{13}$$

The above equations thus provide the amplitude of the enriched degree of freedom, χ, the modification of the initial degrees of freedom induced by the addition of the enrichment, a, and the residual gain, G. The latter quantity is to be used to evaluate the relevance of the proposed enrichment.

3.4 Simplified approach

In the following, the enriched degree of freedom is a displacement field due to the presence of a small and localized crack. It has a small support as compared to the previously introduced degrees of freedom (rigid body motion and uniform strains). Hence the enrichment is expected to be decoupled from the standard degrees of freedom. More generally, when the test function is extended over a large domain, a similar decoupling is to be expected if $\boldsymbol{\Psi}$ is orthogonal to the original basis, *i.e.,* $\int \boldsymbol{\Psi}(\boldsymbol{x}) \cdot \boldsymbol{\Phi}_i(\boldsymbol{x}) \, \mathrm{d}\boldsymbol{x} = 0$. In such a case, it is expected that

$$|P| \gg |\boldsymbol{N}^t \mathbf{M}^{-1} \boldsymbol{N}| \tag{14}$$

This analysis motivates a simplified approach where the amplitude χ and residual gain G are approximated by

$$\begin{aligned} \chi &= \frac{c}{P} \\ G &= \frac{c^2}{2P} \end{aligned} \tag{15}$$

and hence, the two quantities c and P are the only (new) relevant quantities to be computed.

3.5 Fast sensitivity analysis

In the following, not only is the enriched field local, but its shape is the same for all possible locations of the microcrack center, $\boldsymbol{\xi}$. Moreover, changing the microcrack length L can be written as a simple rescaling of a reference test function. From now on, $\boldsymbol{\Psi}$ function will refer to the enriched field corresponding to a microcrack centered at the origin of the coordinate system,

and with a unit length. Therefore, the most general trial field is written as $\boldsymbol{\Psi}((\boldsymbol{x}-\boldsymbol{\xi})/L)$.

The two quantities P and c, are rewritten as

$$P(\boldsymbol{\xi},L)=\int\left[\boldsymbol{\Psi}\left(\frac{\boldsymbol{x}-\boldsymbol{\xi}}{L}\right)\otimes\boldsymbol{\Psi}\left(\frac{\boldsymbol{x}-\boldsymbol{\xi}}{L}\right)\right]:[\boldsymbol{\gamma}(\boldsymbol{x})\otimes\boldsymbol{\gamma}(\boldsymbol{x})]\ \mathrm{d}\boldsymbol{x} \tag{16}$$

and

$$c(\boldsymbol{\xi},L)=\int\left[\boldsymbol{\Psi}\left(\frac{\boldsymbol{x}-\boldsymbol{\xi}}{L}\right)\cdot\boldsymbol{\gamma}(\boldsymbol{x})\right][f(\boldsymbol{x})-\hat{h}(\boldsymbol{x})]\ \mathrm{d}\boldsymbol{x} \tag{17}$$

Both P and c can be evaluated by resorting to Fourier transforms, which will reveal efficient to scan over all positions $\boldsymbol{\xi}$. Let us introduce the Fourier transform $\widetilde{f(\boldsymbol{k})}=\mathcal{F}[f](\boldsymbol{k})=\int f(\boldsymbol{x})\exp(-i\boldsymbol{k}\boldsymbol{x})\ \mathrm{d}\boldsymbol{x}$, and the following notations

$$\begin{aligned}\boldsymbol{\lambda}(\boldsymbol{x}) &\equiv\boldsymbol{\gamma}(\boldsymbol{x})[f(\boldsymbol{x})-\hat{h}(\boldsymbol{x})]\\ \boldsymbol{\Psi}_s(\boldsymbol{x}) &\equiv\boldsymbol{\Psi}(\boldsymbol{x})\otimes\boldsymbol{\Psi}(\boldsymbol{x})\\ \boldsymbol{\gamma}_s(\boldsymbol{x}) &\equiv\boldsymbol{\gamma}(\boldsymbol{x})\otimes\boldsymbol{\gamma}(\boldsymbol{x})\end{aligned} \tag{18}$$

In Fourier space, P and c are simple products

$$\begin{aligned}\widetilde{P(\boldsymbol{k},L)} &=-L\widetilde{\boldsymbol{\Psi}_s(-\boldsymbol{k}L)}:\widetilde{\boldsymbol{\gamma}_s(\boldsymbol{k})}\\ \widetilde{c(\boldsymbol{k},L)} &=-L\widetilde{\boldsymbol{\Psi}(-\boldsymbol{k}L)}\cdot\widetilde{\boldsymbol{\lambda}(\boldsymbol{k})}\end{aligned} \tag{19}$$

and finally

$$\begin{aligned}\chi(\boldsymbol{\xi},L) &=-L\frac{\mathcal{F}^{-1}\left[\mathcal{T}_L[\overline{\mathcal{F}[\boldsymbol{\Psi}]}]\mathcal{F}[\boldsymbol{\lambda}]\right]}{\mathcal{F}^{-1}\left[\mathcal{T}_L[\overline{\mathcal{F}[\boldsymbol{\Psi}_s]}]:\mathcal{F}[\boldsymbol{\gamma}_s]\right]}\\ G(\boldsymbol{\xi},L) &=-\frac{L}{2}\frac{\left(\mathcal{F}^{-1}\left[\mathcal{T}_L[\overline{\mathcal{F}[\boldsymbol{\Psi}]}]\cdot\mathcal{F}[\boldsymbol{\lambda}]\right]\right)^2}{\mathcal{F}^{-1}\left[\mathcal{T}_L[\overline{\mathcal{F}[\boldsymbol{\Psi}_s]}]:\mathcal{F}[\boldsymbol{\gamma}_s]\right]}\end{aligned} \tag{20}$$

where $\mathcal{F},\mathcal{F}^{-1},\mathcal{T}_L$ denote respectively the Fourier, inverse Fourier, and scale operator. Finally, both sought fields χ and G are computed for all center

positions $\boldsymbol{\xi}$ and scale factors L based on fast Fourier transforms. This procedure thus reveals extremely efficient and allows in particular to scan for $\boldsymbol{\xi}$ at all individual pixel positions in a very affordable time (figures are given in the following).

4 Practical approach

The present section now addresses the practical implementation of the above algorithm for the specific goal of identifying microcracks.

4.1 Description of the crack field $\boldsymbol{\Psi}$

It is recalled that $\boldsymbol{\Psi}$ is the displacement field for a microcrack centered at the origin, and of unit extension. The choice of a unique trial displacement field for crack detection is a "simplifying" assumption since the depths of microcracks are broadly scattered. This hypothesis does not seem to prevent a good detection of microcracks at their actual location. But it could be a source of error for crack length and opening quantification. Another assumption in the choice of test field is the crack orientation. Very short microcracks are oriented along the direction of maximum shear stress (stage I propagation [27]). In the present case, it was chosen to focus only on mode I cracks (stage II) that are longer and orthogonal to the load axis. Thus, a *unique* crack test field $\boldsymbol{\Psi}$ is used and the displacement is restricted to its component along the load direction. Oblique cracks could be addressed by following the same strategy (*i.e.,* using several suited crack fields). This extension was not considered in the present study.

An approximation of the latter field can be obtained through an elastic finite element computation. The elastic computations can only provide an approximation of the crack displacement field as the material considered in the experiments reported herein presents a global plastic strain in fatigue (even for low fatigue levels). Moreover, the in-depth geometry (or aspect ratio) of the different initiated microcracks are unknown and presumably randomly distributed. Therefore, several elastic computations with different aspect ratios e ($e = 2d/L$ where d is the crack depth) have been tested. The length is constant ($L = 400\mu m$) and the depth d varies such that e ranges from 0.25 to 2. Plane symmetry conditions are imposed on the horizontal crack plane $(0, y)$ (except on the crack surface), on the vertical plane $(0, x)$ normal to the crack length and that crosses the crack at its center O, and finally on the vertical plane $(0, z)$ normal to the crack depth and that is located 4 mm under the crack in the z direction. Finally a 200 MPa normal compressive stress is prescribed on the crack surface in order to directly reveal the residual elastic displacement field that would superpose to the elastic homogeneous field obtained in the simulation of a sound body submitted to a 200 MPa uniaxial stress. All simulations for the different aspect ratios are run with quadratic finite elements. The geometry, mesh and FE U_x displacement results are illustrated in Figure 3 for $e = 1$.

The displacement fields obtained with the selected aspect ratios are interpolated by

$$\mathbf{\Psi}(x, y) = \Psi(x, y)\mathbf{e}_x = [\mathbf{H}(x) - 1/2]\ \max(\alpha, 0) \tag{21}$$

with x being the direction normal to the crack mouth and

$$\alpha = \sqrt{a_1 + a_2 y^2}\ (a_3 + a_4 x + a_5 x^2)\ \exp[-a_6|x|]\ (A - y^2)\ (B - x^2) \qquad (22)$$

and where $A = B = 1.5$ and $[a_1, ...a_6]$ are adjustable parameters. The component of the displacement parallel to the crack length is neglected so that vector $\boldsymbol{\lambda}$ and tensor $\boldsymbol{\Psi}_s$ reduce to a single component thus saving further on the computation time. The different normalized displacement fields are shown in Figure 4.

For larger aspect ratios e, the computed solution tends to the elastic case of a crack in an infinite plate. This analytical displacement field surrounding the crack is computed from Kolossov-Muskhelishvili potentials φ and ψ in the complex plane $\zeta = x + iy$ [28]

$$\varphi(\zeta) = \frac{\sigma}{2}[\sqrt{\zeta^2 - a^2} - z] \qquad (23)$$

and

$$\psi(\zeta) = -\frac{\sigma a^2}{2\sqrt{\zeta^2 - a^2}} \qquad (24)$$

with

$$U_x + iU_y = \frac{1}{2\mu}[\kappa\varphi(\zeta) - \zeta\overline{\varphi'(\zeta)} - \overline{\psi(\zeta)}] \qquad (25)$$

with $a = L/2$ and under the plane stress assumption

$$\kappa = \frac{3 - \nu}{1 + \nu} \qquad (26)$$

where ν denotes Poisson's ratio.

The (computed) normalized field is interpolated by the function defined in Equation (21) and shown in Figure 5. One trial field has finally been chosen corresponding to a representative crack with a fixed aspect ratio of 2

(Figure 4). This field is also very close to the one obtained analytically and shown in Figure 5. This solution gives the best result for crack quantification (see Section 5.2.1). The crack depth of the chosen aspect ratio should not be seen as a realistic estimate as plasticity effects are neglected. Hence, the crack depth results are not to be interpreted as a measurement in the sequel. Simply, this aspect ratio allows us to obtain a good approximation of the observed displacement field surrounding microcracks. This field can be translated to the position of the assumed crack $\boldsymbol{\xi} = [x_c \; y_c]$ and scaled to the lateral extension of the crack L.

4.2 Crack quantification

The residual gain field gives directly the position of the center of the detected crack. The maximum opening is obtained on the opening field at the coordinate of the center given by the gain map. Finally only the length of the crack remains to be identified.

Let us assume that the image contains a unique well-known crack with a length L_0 in the center of the image such that $\boldsymbol{U}_0(\boldsymbol{x}) = 0$, and $\hat{h} = g = f(\boldsymbol{x}) + \boldsymbol{U}(\boldsymbol{x}, L_0) \cdot \boldsymbol{\gamma}(\boldsymbol{x})$. Hence

$$f(\boldsymbol{x}) - \hat{h}(\boldsymbol{x}) = \boldsymbol{U}(\boldsymbol{x}, L_0) \cdot \boldsymbol{\gamma}(\boldsymbol{x}) \tag{27}$$

Each trial field $\boldsymbol{\Psi}$ corresponds to one particular trial length L and

$$\boldsymbol{\Psi}(\boldsymbol{x}) = \boldsymbol{U}(\boldsymbol{x}, L) \cdot \boldsymbol{\gamma}(\boldsymbol{x}) \tag{28}$$

Then

$$P = \int [\boldsymbol{\Psi}(\boldsymbol{x}, L)]^2 \, \mathrm{d}\boldsymbol{x} \tag{29}$$

and

$$c = \int \boldsymbol{\Psi}(\boldsymbol{x}, L)\boldsymbol{\Psi}(\boldsymbol{x}, L_0)\ \mathrm{d}\boldsymbol{x} \tag{30}$$

Defining the scalar product between two vector fields $\boldsymbol{a}$ and $\boldsymbol{b}$ as

$$\boldsymbol{a} \bullet \boldsymbol{b} \equiv \int (\boldsymbol{a} \otimes \boldsymbol{b}) : (\boldsymbol{\gamma} \otimes \boldsymbol{\gamma})\ \mathrm{d}\boldsymbol{x} \tag{31}$$

its expected value over the local image texture reads

$$\langle \boldsymbol{a} \bullet \boldsymbol{b} \rangle = \langle \boldsymbol{\gamma}^2 \rangle \int \boldsymbol{a} \cdot \boldsymbol{b}\ \mathrm{d}\boldsymbol{x} \tag{32}$$

where the statistical independence of the local image gradient $\boldsymbol{\gamma}$ and trial fields location $\boldsymbol{a}$ or $\boldsymbol{b}$ was exploited.

The expected value of c depends on

$$\langle \boldsymbol{U}(L) \bullet \boldsymbol{U}(L_0) \rangle = \langle \boldsymbol{\gamma}^2 \rangle \int \boldsymbol{U}\left(\frac{\boldsymbol{x}}{L}, 1\right) \cdot \boldsymbol{U}\left(\frac{\boldsymbol{x}}{L_0}, 1\right)\ \mathrm{d}\boldsymbol{x} \tag{33}$$

Introduction of the scaled variable $\mathbf{X}$,

$$\boldsymbol{X} = \frac{\boldsymbol{x}}{L} \tag{34}$$

allows us to rewrite the above scalar product as

$$\langle \boldsymbol{U}(L) \bullet \boldsymbol{U}(L_0) \rangle = \langle \boldsymbol{\gamma}^2 \rangle L \int \boldsymbol{U}(\boldsymbol{X}, 1) \cdot \boldsymbol{U}\left(\boldsymbol{X}\frac{L}{L_0}, 1\right)\ \mathrm{d}\boldsymbol{X} \tag{35}$$

where

$$C(L/L_0) = \int \boldsymbol{U}(\boldsymbol{X}, 1) \cdot \boldsymbol{U}\left(\boldsymbol{X}\frac{L}{L_0}, 1\right)\ \mathrm{d}\boldsymbol{X} \tag{36}$$

finally

$$\langle G \rangle = \langle \gamma^2 \rangle L\ \frac{C(L/L_0)^2}{2C(1)} \tag{37}$$

Function $C(L/L_0)$ is the cross correlation product between the trial displacement field ($\boldsymbol{U}(L)$) and the crack displacement field ($\boldsymbol{U}(L_0)$). Consequently,

C presents a maximum for $L/L_0 = 1$. The extra factor L in the right-hand side of Equation (37) shows that there is a natural "bonus" on the gain G due to the sole size of the test function, and hence directly looking for the maximum gain tends to favor an overestimation of L. Rather, the variable

$$G_{norm} = \frac{G}{L} \tag{38}$$

will be maximum for $L = L_0$. Therefore, in order to identify both the location and the length of a microcrack, one should look for the maximum of G_{norm} over $\boldsymbol{\xi}$ and L. To get directly the position of the center and the length of the crack, the computed gain field is replaced by G_{norm}.

4.3 Numerical test with a single crack

In this section, the results are presented for a synthetic case in which one microcrack is artificially introduced in the reference image (first image of the test corresponding to 0 cycle or undamaged state). In that case, the parameters of the crack (size, opening and location) are known. The displacement field applied to the reference picture is shown in Figure 6.

The numerically deformed image is then normally used as the damaged image for the correlation code. The resulting fields are shown in Figure 7. Both fields present a peak at the center of the crack for coordinates [750 750] pixels. The computed opening (see Figure 7(b)) at the center coordinates is equal to 0.48 pixel (to be compared with the prescribed value of 0.5 pixel). Finally, Figure 8 shows the change with respect to the trial length L of the computed gain G_{norm} at the center crack position. A peak is well defined for $L = 50$ pixels.

One of the objectives of the method was the low computation cost. In this numerical test, the computation time on a basic laptop is 3 s for a region of 360×360 pixels and for 20 trial lengths. (Note that this computation cost is *independent* of the number of microcracks present in the examined images.)

4.4 Case of multiple crack detection and quantification

An algorithm is developed in order to detect multiple microcracks on real images. This implies that multiple maxima of the normalized gain field are to be looked for. However, the unavoidable presence of noise will always produce a large number of local maxima in G_{norm}, even if no microcracks are present. Therefore, a thresholding procedure has to be designed to distinguish meaningful from spurious maxima. One additional difficulty is that the image texture naturally induces spatial heterogeneities in the noise sensitivity. Hence, the threshold level should be a heterogeneous field.

To evaluate this sensitivity, the above procedure is applied to compute G and χ between the reference image, and a few ones taken at a very early stage of the experiment where no microcracks are expected. These sets of experimental image pairs are representative of the basic noise that is present in the entire image series. It reveals useful to combine two thresholds, namely one on the gain, G_{norm}, and a second one on the opening, χ. Thus for the first sets of image pairs, both fields, denoted by $G^0(\boldsymbol{\xi}, L)$ and $\chi^0(\boldsymbol{\xi}, L)$, are recorded.

An example is taken from a real test at ± 190 MPa. The first image of the test is the reference one, then the three following images are used to

compute threshold data. The maps are shown for $L = 120$ pixels in Figure 9. Once those fields are computed, the identification of microcracks from the pair of fields G_{norm} and χ makes use of a binary mask, M_{mask}, which is the intersection of the thresholded gain and opening. $M_{mask}(\boldsymbol{\xi}, L) = 1$ if and only if $G_{norm}(\boldsymbol{\xi}, L) > K_1 \langle G^0(\boldsymbol{\xi}, L) \rangle$ and $\chi(\boldsymbol{\xi}, L) > K_2 \max(\chi^0(\boldsymbol{\xi}, L))$ (where the average $\langle ... \rangle$ and "max" operator respectively denote the average and maximum value over the three considered images), and $M_{mask}(\boldsymbol{\xi}, L) = 0$ otherwise. In those expressions K_1 and K_2 are constants that are tuned to adjust the sensitivity of the procedure. In the following, the chosen values are $K_1 = 25$ and $K_2 = 1$. An example of the binary matrix M_{mask} will be shown further down (Figure 12a). Microcracks are then identified as local maxima within the domain where $M_{mask} = 1$.

Finally in order to avoid the multiple count of cracks, it is assumed that an area of $x = L/2$ and $y = L$ around an already detected crack cannot contain another crack center. This implies another assumption in crack detection, namely the cracks have to be far enough from one another to be considered as genuine ones.

5 Practical application of the method

5.1 Single image computation

The observed noise level is first linked to the sensitivity of the sensor and second, to the surface change during the first step of the test mainly due to PSB initiations. Consequently, the level of noise should grow with damage

growth.

For the computation, the central part of the 13th image is chosen (corresponding to 120,000 cycles while $N_F = 145,000$ cycles). First the long wavelength displacement field computation is carried out with the global DIC technique as above described using uniform strains and rotations. The displacement field along the x axis (Figure 10(a)) and correlation residual (Figure 10(b)) are the main outputs of this first step. The displacement gradient is due to cyclic softening. The deformed image is then corrected to provide the input $\hat{h}$ image of the sensitivity analysis. No microcrack is detected on the residual field map. Only boundaries of the ferritic grains are observed.

Then, gain G_{norm} and opening χ values are computed at each pixel and for 11 trial lengths (ranging from 30 to 130 pixels with a 10-pixel step). One result is presented for $L = 120$ pixels (Figure 11). The maps show a high level of noise but multiple peaks appear. In order to isolate the cracks, mask M_{mask} is computed and shown in Figure 12(a). To illustrate the final result, the global displacement field is reconstructed adding the first order long wavelength field to the local fields surrounding detected microcracks (Figure 12(b)). In Figure 12(b) a white square defines the possible zone of crack centers. A crack center cannot exist on the boundaries as the trial displacement field used for detection would leave the computed area. Finally, the selected zone seems to contain 6 cracks whose length varies from 50 pixels (*i.e.,* 150 μm) to 110 pixels (*i.e.,* 350 μm) and with openings ranging from 0.25 pixel (*i.e.,* 0.8 μm) to 0.5 pixel (*i.e.,* 1.6 μm). The detection threshold can be seen as the minimum resolvable crack opening. This threshold mainly

depends on the texture quality (and on the choice of parameters K_1 and K_2). The different tests performed showed that the level of noise prevent any detection of cracks with an opening less than 0.2 pixel (*i.e.,* 0.6 μm). The main part of the computation time is for the first global evaluation that takes about 30 s for a 600×600-pixel region. Crack detection itself is performed in 13 s with 20 trial lengths.

For comparison purposes, it is also possible to use Q4-DIC [25]. This type of computation is not dedicated to crack detection. It computes the displacement fields as a decomposition over a finite element basis of shape functions (4-noded quadrilateral elements, or Q4, on a regular square mesh with a bilinear variation of the shape functions over the elements). The same couple of images as before is used and the displacement field along the x-axis is shown in Figure 13(a). This result can directly be compared to the final reconstructed field in Figure 12(b).

The same type of global displacement gradient is found and some discontinuities interpreted as microcracks that are read from the displacement map. A way to make them more visible is to perform a Q4-DIC analysis between the 4th image and the same (13th) damaged image. The uniform strain is then close to zero as the change of the cyclic behavior of the material is now small between these two pictures. The result is shown in Figure 13(b). The time for performing the Q4-DIC computation is around 4 min and it does not directly give quantitative data concerning the number of cracks, their length and opening. Although they can be guessed when their size and opening are large, the level of noise remains high since the entire displacement range is less than 1 pixel for the entire image. A small element size has to be used

to detect the microcracks, here as small as 4-pixel wide. For larger elements (such as 32×32 pixels) no cracks could be detected. Last, the positions of the cracks between Q4-DIC and the automatic detection technique are compared in Figure 14. A good agreement is observed.

5.2 Multiple image computation

5.2.1 Propagation curves

For very low fatigue loading close to the fatigue limit, few microcracks initiate on the surface of the specimen. One test has been performed in this regime ($\pm$180 MPa). Every 10,000 cycles the method is used with the first image of the test corresponding to 0 cycle at maximum load. For this type of test, replicas have been performed. It is thus possible to compare DIC estimates of the length and opening of the cracks with the results obtained using the latter technique. The result at 300,000 cycles for Q4-DIC is illustrated in Figure 15(a). This number of cycles corresponds to the limit of detection in Q4-DIC. One will notice (see Figure 17a) that the new presented crack detection technique allows the detection of the crack 50,000 cycles before Q4-DIC. The observation of the central microcrack over the replica is shown in Figure 15(b). Last, the result obtained with the crack detection technique is presented in Figure 16.

The comparison of several images is plotted in Figure 17. Figure 17a shows the change of the crack length with the number of cycles. The replication technique is the most sensitive in terms of resolution. One evaluated error bar ($\pm 5\mu$m) is plotted for 400,000 cycles. The Q4-DIC points are ob-

tained by "manual" evaluation of the length from the displacement maps (one example is given in Figure 15(a)). As a consequence the error on crack quantification has been evaluated to amount to ± 20 pixels, which corresponds to $\pm 64\mu$m (see corresponding error bars in Figure 17(a)). The Q4-DIC evaluation (which requires about 10-minute computation time) for each image tends to under-evaluate the real length of the crack. The results obtained with the proposed method are also plotted. The error bars correspond to the discretization on the length evaluation (here ± 8 pixels or $\pm 24\mu$m). The results are very close to those of the replicas when the crack is very short. Then the technique (consisting in a first and fast evaluation) tends to overestimate the crack length. This analysis has only been performed over a unique crack in one loading case. Moreover, one major simplifying assumption is the use of an elastic crack field $\boldsymbol{\Psi}$ for crack detection while the material behavior is known to be elasto-viscoplastic. In the presence of plasticity, a blunting of crack tips is expected, which contributes to increase the crack opening on all the crack length contrary to an elastic field for which this opening vanishes at the crack tip. Therefore the actual displacement field around a crack should be different from the one proposed by the elastic theory. As a consequence, it is natural to overestimate the crack length initiated in a plastic material if an elastic field is chosen as the perturbation displacement field. But even with such a rough approximation of the displacement field, it is possible to estimate the crack length. In order to obtain a more precise length or opening value, other computations may be performed around the detected crack.

Another interesting result is the detection of the number of cycles for

crack initiation. Since the test was expected to last about one million cycles, replicas were performed every 100,000 cycles. The first detection with the replica technique is obtained for 300,000 cycles. Image capture can be performed more frequently (here every 10,000 cycles) as its cost is negligible. Initiation detection with Q4-DIC is estimated around 300,000 cycles (see Figure 15(a)). The best result is obtained by the automatic detection technique which gives a crack initiation at 230,000 cycles.

The comparison of the crack opening history is shown in Figure 17(b). The evaluation of the opening over the replicas is not as accurate as the length evaluation. First, the replicas are made after the creep of the specimen [29]. Second, the opening changes along the crack length in a very chaotic fashion because of the underlying grain microstructure and possible merging of smaller microcracks, or microcrack impregnation with the replica coating. Hence, the opening has been evaluated at the center of the microcrack. Large error bars (no precise quantification have been performed) should be present in Figure 17(b)). A rough evaluation of the uncertainty is around ± 1 μm. The quantification of the opening with the detection technique is also very difficult since the crack aspect ratio is very different from the theoretical one. Yet the results are quite close (± 1.5 μm). This confirms that the technique proposed herein is able to give a first estimation of the crack opening even for very short cracks with an estimated resolution of the order of 0.2 pixel (*i.e.,* 600 nm).

5.2.2 Crack density

Images from the same test (±190 MPa) are used but contrary to Section 4.4, the whole image is considered in the computation (1500×1100 pixels) that is repeated for all images captured during the test. A first phase is the evaluation of the level of noise in the whole image using the threshold computation. The computation is then performed with $K_1 = 25$ and $K_2 = 1$.

An example of the reconstructed field is given after 120,000 cycles in Figure 18(a) and compared with a Q4-DIC result in Figure 18(b). For each image pair, the crack density is computed as the number of cracks divided by the analyzed area. The crack density change with the number of cycles obtained with the present automatic detection is plotted in Figure 19. This result is compared to that obtained by "manual count" in displacement maps obtained with Q4-DIC. The error that can be done by manual counting remains small. It depends on the number of initiated cracks. The major part of microcracks with $L > 150$ μm are detected. However the Q4-DIC computations with an element size of 4×4 pixels are very long to perform and require a powerful computer. The error with the automatic detection is mainly due to the choice of the sensitivity parameters K_1 and K_2. Several tests have been conducted with different values of K_1 and K_2 in the case of numerous crack initiations. The automatic detection seems to overestimate the crack density but some cracks are too long to be detected as a single one and are then detected as two microcracks. This is due to the limit numerically imposed on crack length evaluation (*i.e.,* 130 pixels herein). Moreover, as the noise level grows with damage, the method tends to detect "ghost" cracks

that are only noise. Overall, the automatic detection allows for a reliable quantification for crack density evolution at very small computational costs.

6 Summary

In this paper a novel global DIC-based method is proposed to detect and quantify automatically microcracks initiating at the surface. This issue is quite challenging as typical crack openings are in the range 0.1 to 0.5 pixel, and extensions varying between 50 and 150 pixels. Moreover, as the trial displacement field is assumed to be invariant up to a translation of the microcrack position, a Fast Fourier Transform is proposed for a very efficient scanning of the position of the microcracks. Application of the technique to an experimental case revealed a very good ability to detect and locate microcracks. A crack detection threshold of 0.2 pixel (*i.e.,* 0.6 μm) for crack opening has been experimentally observed.

At the present stage, the estimate of crack length and opening remains qualitative, which may be attributed to an approximate trial field based on the assumption of a fixed aspect ratio for the unknown in-depth geometry of the cracks and elastic behavior. This last point is known to be a rough approximation for the material studied herein (304L stainless steel). Conversely, the estimate of the crack density was shown to be very reliable. This quantity is one of the experimental inputs for models accounting for multiple initiations [10], subsequent propagation and shielding [30].

Finally, it is to be stressed that the present methodology can be extended to any local alteration of the surface whose signature in terms of displacement

field can be described faithfully by a test function with a compact support.

References

[1] Ewing JA, Humfrey JCW. The fracture of metals under repeated alternations of stress. *Phil Trans Royal Society*. 1903; CC:241–250.

[2] Magnin T, Coudreuse L, Lardon JM. A quantitative approach to fatigue damage evolution in FCC and BCC stainless-steels. *Scripta Metallurgica*. 1985; 19:1487–1490.

[3] Ochi Y. An experimental and statistical investigation of surface fatigue crack initiation and growth. *Fatigue and Fracture of Engineering Materials and Structures*. 1985; 8:327–339.

[4] Hoshide T, Socie DF. Crack nucleation and growth modeling in biaxial fatigue. *Engineering Fracture Mechanics*. 1988; 29:287–.

[5] Chauvot C, Sester M. Fatigue crack initiation and crystallographic crack growth in an austenitic stainless steel. *Computational Materials Science*. 2000; 19:87–96.

[6] El Bartali A, Aubin V, Degallaix S. Fatigue damage analysis in a duplex stainless steel. *Fatigue and Fracture of Engineering Material and Structures*. 2008; 31:137–151.

[7] Sutton MA, Zhao W, McNeill SR, Helm JD, Piascik RS, Riddel WT. Local crack closure measurements: Development of a measurement system using computer vision and a far-field microscope. *Advances in*

fatigue crack closure measurement and analysis: second volume, STP 1343. 1999; 145–156.

[8] Polak J, Zezulka P. Short crack growth and fatigue life in austenitic-ferritic duplex stainless steel. *Fatigue and Fracture of Engineering Materials and Structures*. 2005; 20:923–935.

[9] Malésys N. Modélisation probabiliste de la formation de réseaux de fissures en fatigue thermique. *Phd thesis*. 2007.

[10] Rupil J, Vincent L, Hild F, Roux S. Identification and probabilistic modeling of mesocrack initiations in 304L stainless steel. *International Journal for Multiscale Computational Engineering*. 2011; in press.

[11] McNeill SR, Peters WH, Sutton MA. Estimation of stress intensity factor by digital image correlation. *Eng Fract Mech*. 1987; 28:101–112.

[12] Sutton MA, Helm JD, Boone ML. Experimental study of crack growth in thin sheet 2024-T3. *International Journal of Fracture*. 2001; 109:285–301.

[13] Abanto-Bueno J, Lambros J. Investigation of crack growth in functionally graded materials using digital image correlation. *Eng Fract Mech*. 2002; 69:1695–1711.

[14] Hamam R, Hild F, Roux S. Stress intensity factor gauging by digital image correlation: Application in cyclic fatigue. *Strain*. 2007; 43:181–192.

[15] Mughrabi H, Wang R, Differt K, Essman U. Fatigue crack initiation by cyclic slip irreversibilities in high-cycle fatigue. *Fatigue mechanisms : Advances in quantitative measurement of physical damage, ASTM STP.* 1983; 811:5–45.

[16] Ma B, Laird C. Overview of fatigue behavior in copper single crystals (parts 1 to 5). *Acta Metallurgica.* 1989; 37(2):325–379.

[17] Man J, Obrtlik K, Blochwitz C, Polak J. Atomic force microscopy of surface relief in individual grains of fatigued 316L austenitic stainless steel. *Acta Materialia.* 2002; 50:3767–3780.

[18] Sutton MA, McNeill SR, Jang J, Babai M. Effects of subpixel image restoration on digital correlation error estimates. *Opt Eng.* 1988; 27[10]:870–877.

[19] Bornert M, Brémand F, Doumalin P, Dupré JC, Fazzini M, Grédiac M, et al. Assessment of Digital Image Correlation measurement errors: Methodology and results. *Exp Mech.* 2009; 49[3]:353–370.

[20] Poncelet M, Barbier G, Raka B, Courtin S, Desmorat R, Le-Roux JC, et al. Biaxial High Cycle Fatigue of a type 304L stainless steel: Cyclic strains and crack initiation detection by digital image correlation. *European Journal of Mechanics A/Solids.* 2010; 29:810–825.

[21] Colin J, Fatemi A, Taheri S. Fatigue Behavior of Stainless Steel 304L Including Strain Hardening, Prestraining, and Mean Stress Effects. *Journal of Engineering Materials and Technology.* 2010; 132:021008,1–13.

[22] Roux S, Hild F. Stress intensity factor measurements from digital image correlation: post-processing and integrated approaches. *International Journal of Fracture*. 2006; 140:141–157.

[23] Roux S, Hild F, Berthaud Y. Correlation Image Velocimetry: A Spectral Approach. *Appl Optics*. 2002; 41[1]:108–115.

[24] Wagne B, Roux S, Hild F. Spectral Approach to Displacement Evaluation From Image Analysis. *Eur Phys J AP*. 2002; 17:247–252.

[25] Besnard G, Hild F, Roux S. Finite element diplacement fields analysis from digital images: Application to Portevin-Le Chatelier bands. *Experimental Mechanics*. 2006; 46:789–803.

[26] Bonnet M, Guzina BB. Sounding of finite solid bodies by way. *Int J Num Meth Eng*. 2004; 61:2344–2373.

[27] Forsyth PJE. A two stage process of fatigue crack growth. *Proc Symp Crack Propagation*. 1961; 76–94.

[28] Bui HD. *Mécanique de la rupture fragile*. Masson, 1978.

[29] Delobelle P. Synthesis of the elastoviscoplastic behavior and modelization of an austenitic stainless steel over a large temperature range, under uniaxial and biaxial loadings, Part 1 : Behavior. *International Journal of plasticity*. 1993; 9:65–85.

[30] Malésys N, Vincent L, Hild F. A probabilistic model to predict the formation and propagation of crack networks in thermal fatigue. *International Journal of Fatigue*. 2009; 31:565–574.

Appendix: list of notations

$[a_1, ...a_6]$: adjustable parameters used for additional test function interpolation

$\mathbf{a^{(p)}}$: estimated components of the displacement field $\boldsymbol{U}$ at step p of the iterative process

a_n^0: initial sought components of the displacement field $\boldsymbol{U}$ over the basis $\boldsymbol{\Phi}_n$

A: adjustable parameter used for additional test function interpolation

$\mathbf{b^{(p)}}$: second member of the global linear system

B: adjustable parameter used for additional test function interpolation

c: additional second member of the linear system corresponding to the additional test function $\boldsymbol{\Psi}$

$C(L/L_0)$: cross correlation product between the trial displacement field $\boldsymbol{U}(L)$ and the crack displacement field $\boldsymbol{U}(L_0)$

d: crack depth

e: crack aspect ratio

$f(\boldsymbol{x})$: reference image

$\widetilde{f(\boldsymbol{k})}$: Fourier transform of function f

$\mathcal{F}$: Fourier transform

$\mathcal{F}^{-1}$: inverse Fourier transform

$g(\boldsymbol{x})$: deformed image

G: detection quality gain field (corresponding to local residual R)

G^0: initial quality gain field

G_{norm}: modified quality gain (normalized by the crack length)

$\hat{h}(\boldsymbol{x})$: corrected deformed image

$\hat{h}^{(p)}(\boldsymbol{x})$: corrected deformed image adjusted at step p of the iterative process

$\mathbf{H}(x)$: Heaviside function

K_1: crack detection sensitivity parameter for quality gain

K_2: crack detection sensitivity parameter for opening

L: microcrack total surface length

L_0: given crack length

$\mathbf{M}$: matrix of the global linear system

M_{mask}: mask used to locate cracks

N: number of degrees of freedom used for the first global displacement field evaluation

N_c: number of cycles

$\mathbf{N}$: additional cross term of the linear system corresponding to additional test function $\boldsymbol{\Psi}$

N_F: number of cycles to failure

P: additional first member of the linear system corresponding to additional test function $\boldsymbol{\Psi}$

R_0: global correlation residual

$\mathcal{T}_L$: scale operator

$\boldsymbol{U}$: in-plane displacement field

U_x: displacement field along x

U_y: displacement field along y

$\boldsymbol{V}$: trial in-plane displacement field

$\boldsymbol{V}^{(p)}$: trial in-plane displacement field adjusted at step p of the iterative pro-

cess

$\boldsymbol{x}$: in-plane spatial coordinates

x: first spatial coordinate

y: second spatial coordinate

z: third spatial coordinate

α: part of the interpolation function for additional crack displacement field function Ψ

γ: reference image gradient

$\boldsymbol{\delta a}^{(p)}$: correction to apply to the current estimate of components $\mathbf{a}^{(\mathbf{p-1})}$ of the displacement field

$\boldsymbol{\delta V}^{(p)}$: correction to apply to the current estimate $\boldsymbol{V}^{(p-1)}$ of the trial displacement field

$\Delta\sigma_{xx}$: controlled stress variation along x axis

ζ: complex plane coordinate

ν: Poisson's ratio

$\boldsymbol{\xi}$: in-plane crack center coordinates

φ: first Kolossov-Muskhelishvili potential

$\boldsymbol{\Phi}_n$: n-function basis for displacement field decomposition

χ: crack opening field

χ^0: initial crack opening field

ψ: second Kolossov-Muskhelishvili potential

Ψ: x-axis component of the additional test function $\boldsymbol{\Psi}$

$\boldsymbol{\Psi}$: additional test function corresponding to local displacement field for a crack centered at the origin and of unit extension

List of Figures

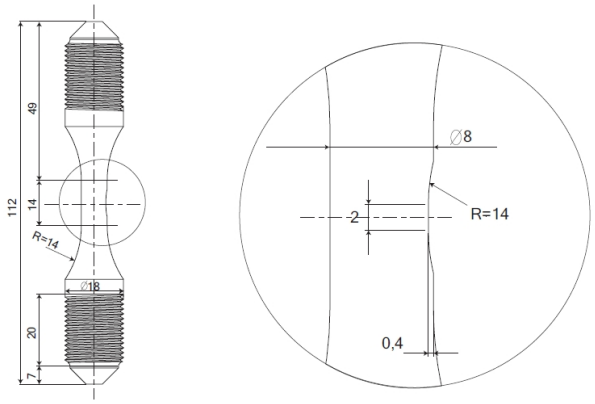

Figure 1: Geometry of the specimen with a flat part (0.4 mm in depth) in the center of the gauge zone [9]. All dimensions are in mm.

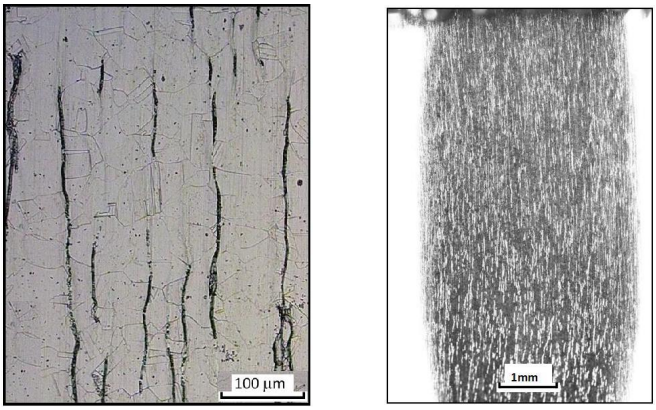

(a) (b)

Figure 2: (a) 304L microstructure made of austenitic grains (gray) with ferritic residual grains (black). (b) Example of raw image captured by macro photography over the notch. The ferrite appears in white in this picture.

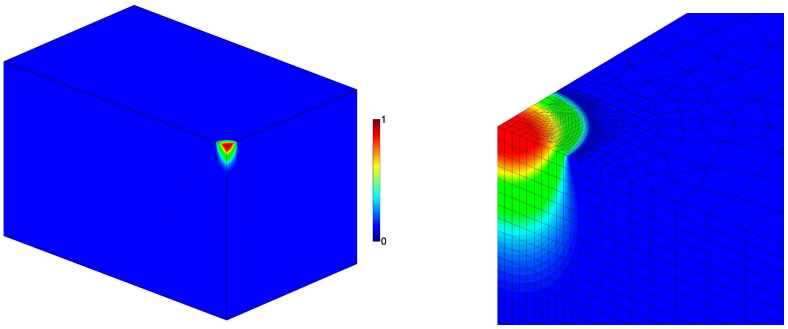

(a) (b)

Figure 3: (a) Geometry for displacement field computations (crack length: 200μm, crack depth: 200μm, total depth: 4 mm, total length: 2.5 mm, total height: 2.5 mm). (b) Displacement field along the direction normal to the crack mouth (normalized) obtained for $e = 1$ and focused around the crack area, 73,600 finite elements are used.

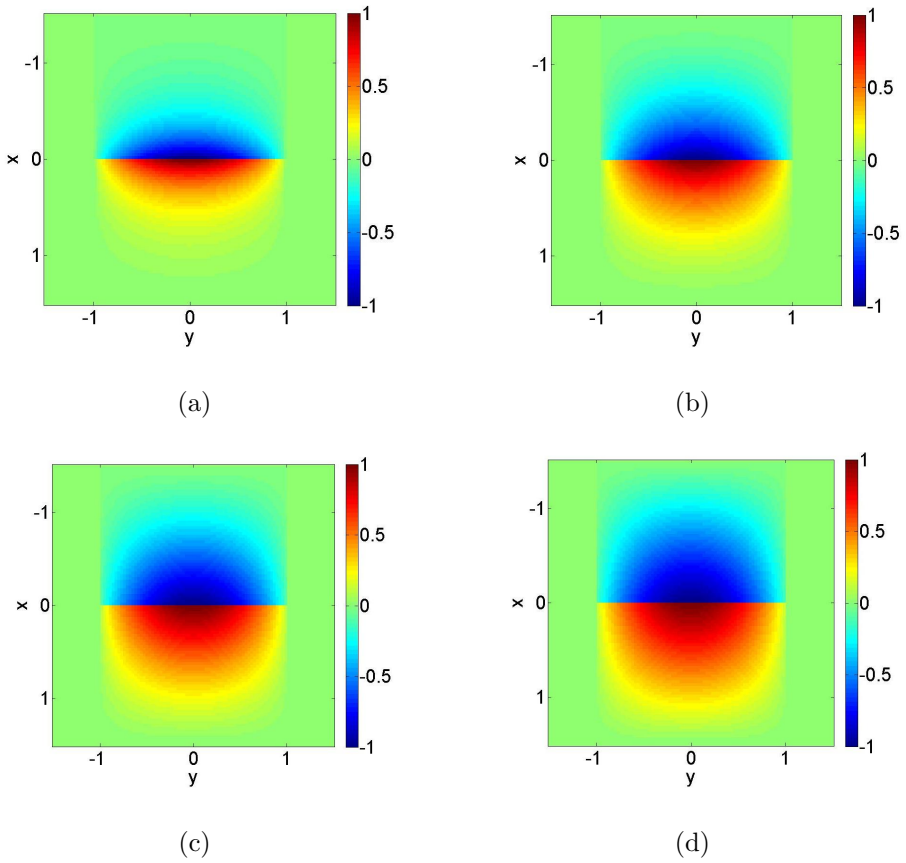

Figure 4: Adjusted displacement field (along direction x) for (a) $e = 0.25$, (b) $e = 0.5$, (c) $e = 1$, (d) $e = 2$.

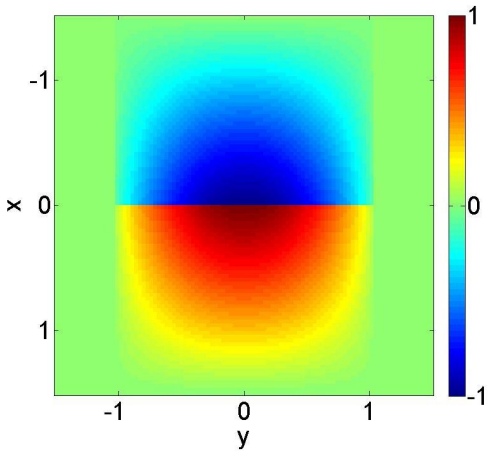

Figure 5: Analytical displacement field $\mathbf{\Psi}$.

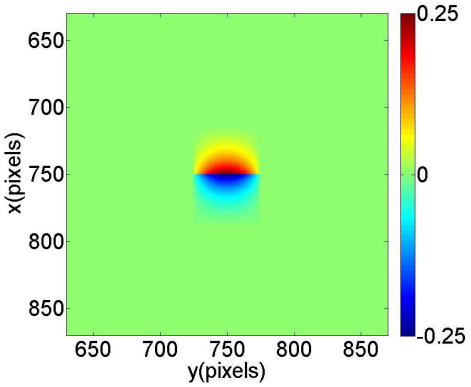

Figure 6: Displacement field in direction x corresponding to a microcrack with the following parameters: $L = 50$ pixels, center=[750 750] pixels and maximum opening = 0.5 pixel.

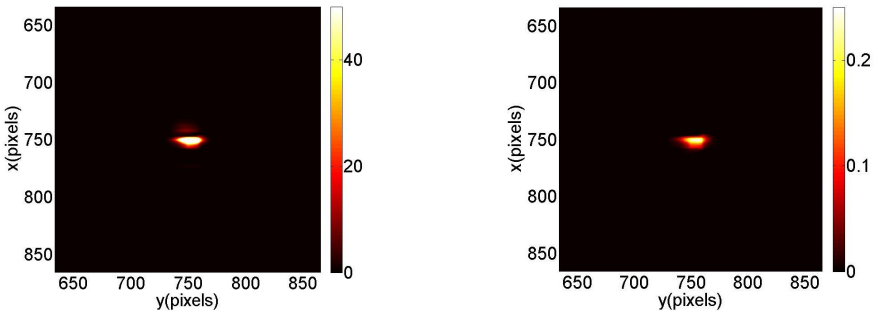

(a) (b)

Figure 7: (a) Quality gain G_{norm} map obtained for a trial length of 50 pixels. (b) Half opening map obtained for a trial length of 50 pixels.

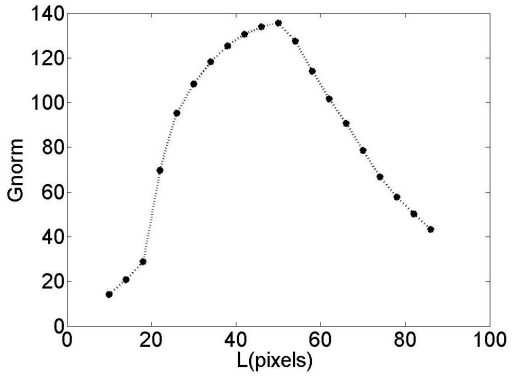

Figure 8: Change of the quality gain G_{norm} for the different trial lengths (for $x = y = 750$ pixels).

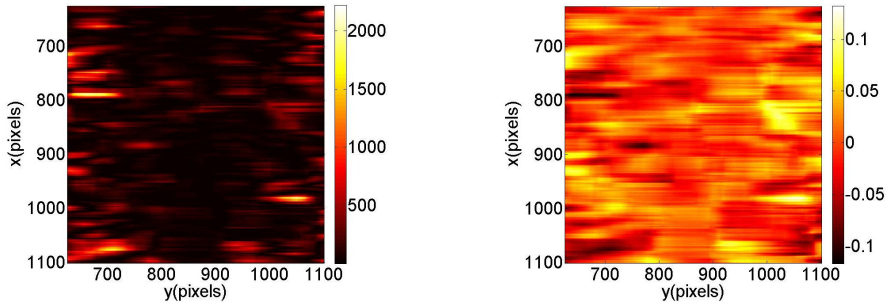

(a) (b)

Figure 9: (a) Threshold gain map computed for a trial length of 120 pixels. (b) Threshold opening map computed for a trial length of 120 pixels (1 pixel $\leftrightarrow$ 3.2 μm).

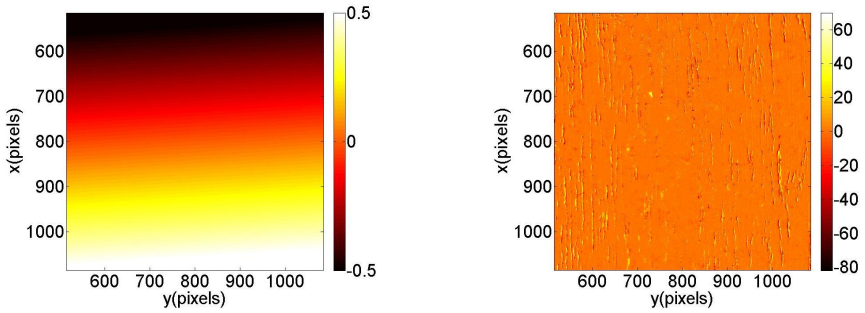

(a) (b)

Figure 10: (a) Measured displacement field (expressed in pixel) along the x-axis by the first global approach (1 pixel $\leftrightarrow$ 3.2 μm). (b) Residual (in gray levels) map obtained after a first global computation.

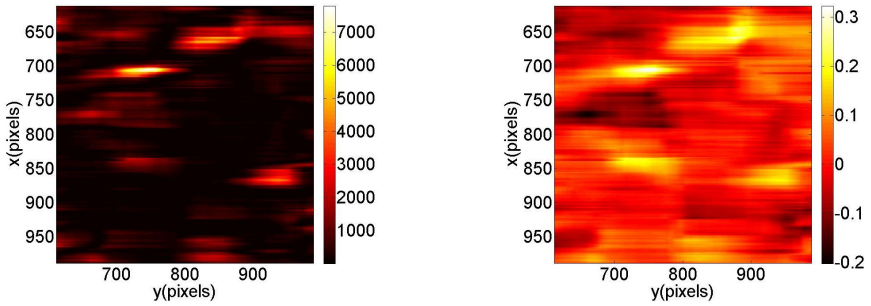

(a) (b)

Figure 11: (a) Gain map for a trial length of 120 pixels. (b) Opening field map for a trial length of 120 pixels (1 pixel $\leftrightarrow$ 3.2 μm).

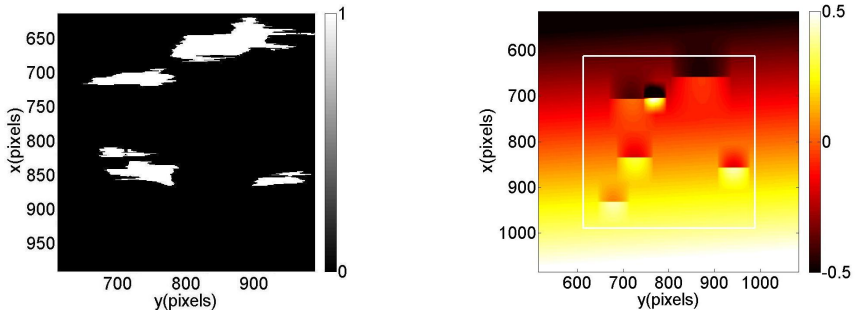

(a) (b)

Figure 12: (a) Binary matrix (M_{mask}) for $L = 120$ pixels. White zones correspond to possible crack locations. (b) Reconstructed displacement field (expressed in pixel) along the x-axis for all analyzed crack lengths (1 pixel $\leftrightarrow$ 3.2 μm).

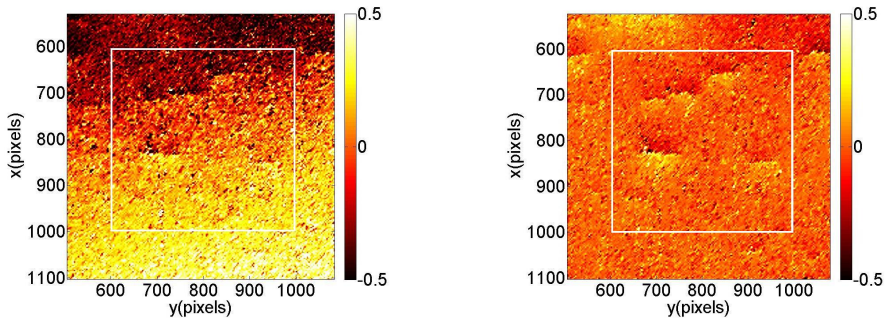

(a) (b)

Figure 13: U_x field obtained with Q4-DIC with 4×4-pixel elements (1 pixel $\leftrightarrow$ 3.2 μm). Deformed image = 120,000 cycles, reference image = 0 cycle (a), and 30,000 cycles (b).

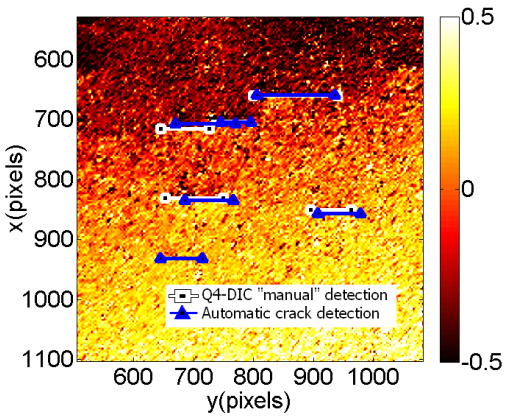

Figure 14: Comparison of the crack positions determined by Q4-DIC ("manual" detection) and the automatic detection technique.

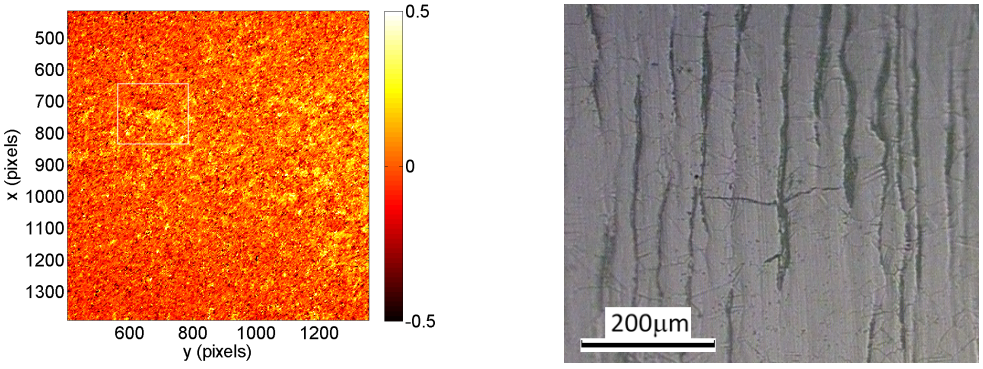

(a) (b)

Figure 15: (a) Displacement field expressed in pixel measured by using Q4-DIC (element size: 4×4 pixels) for $N_c = 300,000$ cycles (1 pixel $\leftrightarrow$ 3.2 μm). (b) Replica observation performed after $N_c = 300,000$ cycles.

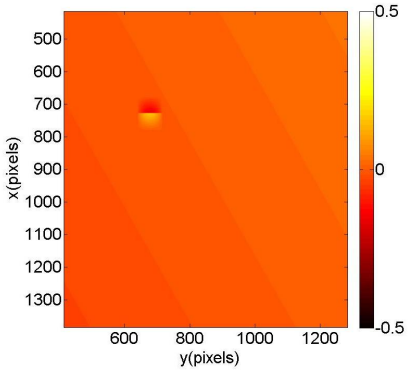

Figure 16: Reconstructed displacement field at $N_c = 300,000$ cycles with the technique developed herein.

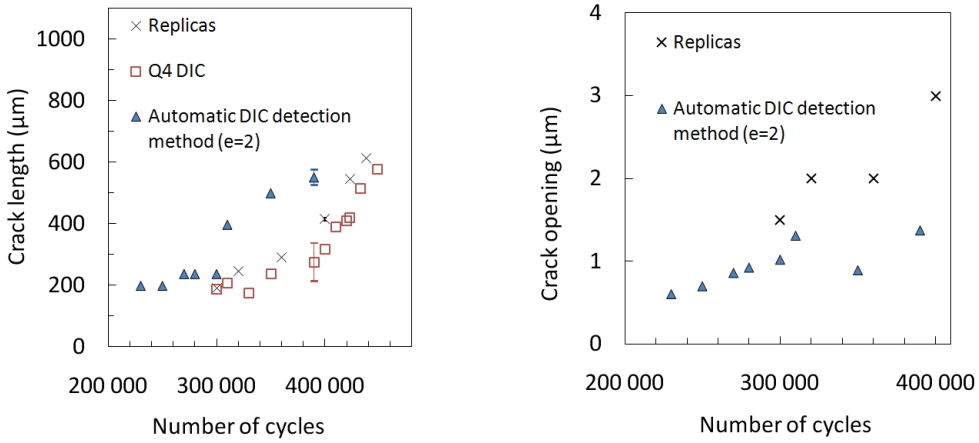

(a) (b)

Figure 17: (a) Crack length and (b) crack opening history of a single microcrack as revealed by three methods: replica (×), Q4-DIC (□), and the proposed method (△).

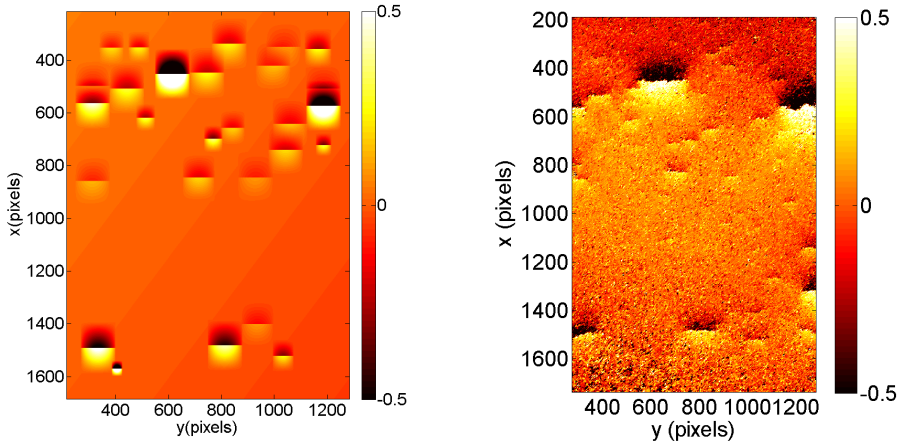

(a) (b)

Figure 18: (a) Reconstructed displacement field U_x (in pixel) after 120,000 cycles. (b) Q4-DIC displacement field U_x (in pixel) at 120,000 cycles (1 pixel $\leftrightarrow$ 3.2 μm).

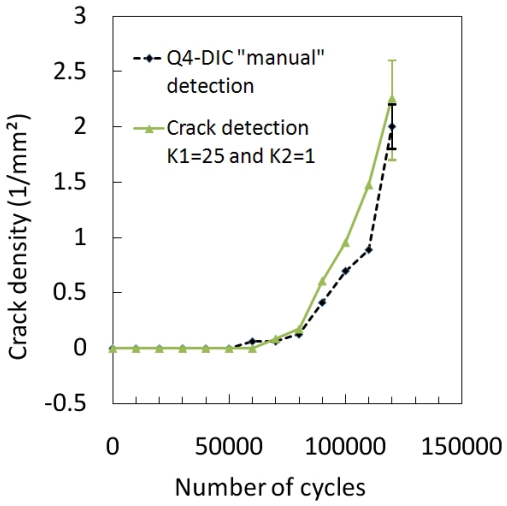

Figure 19: Crack density vs. number of cycles for Q4-DIC "manual" detection (the error bar correspond to an estimation of the number of cracks roughly detected) and automatic detection (the error bar corresponds to the results obtained with different values of $20 < K_1 < 35$ and $0.8 < K_2 < 1.4$).